# Supersolvus Recrystallization and Grain Growth Kinetics for the Fine Tuning of Grain Size in VDM Alloy 780 Forgings

M. HAFEZ HAGHIGHAT, J. SHARMA, B. GEHRMANN, H. ALVES, and N. BOZZOLO

VDM Alloy 780 is a new polycrystalline nickel-based superalloy developed for aeronautical applications. In most of the targeted applications, grain size after forging must be precisely controlled to meet the targeted mechanical properties and in-service life requirements. Grain size in forgings is the direct consequence of the recrystallization and grain growth kinetics which are addressed in this paper at high temperatures, above the solvus temperature of $\gamma'$ and $\eta/\delta$ phases. The dynamic and post-dynamic recrystallization kinetics as well as the grain growth kinetics of VDM Alloy 780 are detailed over a range of thermomechanical conditions. Dynamic recrystallization appears to be limited, with only 30 pct recrystallized at quite high strain of 1.7 applied at 1050 °C and 0.01 $s^{-1}$ for instance, but this is compensated by fast post-dynamic evolution. Within the investigated thermomechanical range, recrystallization is completed with 5 minutes of post-deformation hold in VDM Alloy 780 independent of the prior strain, strain rate and dynamic recrystallization fraction. For a strain as low as 0.08, an isothermal annealing of 30 minutes at 1050 °C generates a homogenous and fully recrystallized microstructure. Capillarity driven grain growth following recrystallization is also relatively slow, for instance an exposure at 1050 °C (50 °C above the solvus temperature) for 2 hours results in an increase in average grain size from 20 to 70 $\mu$m. This opens the possibility to fine tune the grain sizes by subsequent heat treatments within a time scale that is compatible with industrial conditions. The high cobalt content (25 pct) is suspected to play a role in the control of microstructure evolution kinetics. It is noteworthy that VDM Alloy 780 is shown here to not undergo the heterogeneous grain growth phenomenon reported in low strain regions for other nickel-based superalloys, which is also an asset for applications requiring strict control of grain sizes and grain size distributions.

https://doi.org/10.1007/s11661-023-07018-8


## I. INTRODUCTION

NICKEL-BASED superalloys provide excellent properties at elevated temperatures which make them indispensable in aircraft engines especially in low and high-pressure turbine discs but also in other high temperature applications where creep resistance must be guaranteed. Ni-based superalloys constitute almost 40 to 50 pct of the total weight of an aircraft engine.[1] Alloy 718 is still to date the most used turbine disc material due to its ease of processing, mechanical properties, and relatively low cost. The operating temperature of jet engines using Alloy 718 is limited to temperatures close to 650 °C mainly due to its microstructure and the resulting mechanical properties.

Developing new alloys with higher operating temperatures to increase the efficiency of aero engines has been the focus of different studies in the last decades, most of those are strengthened by $\gamma$' phase precipitation. Following this trend, VDM Metals GmbH in collaboration with the Institute for Materials Science in the Technical University of Braunschweig has developed a polycrystalline Ni-based superalloy namely VDM®Alloy 780 aiming service temperatures up to 750 °C. It is aimed to tune the microstructure characteristics for obtaining specific mechanical properties as well as good formability and weldability. These promote VDM Alloy 780 to be employed in different product forms like bars, wires

M. HAFEZ HAGHIGHAT, B. GEHRMANN, and H. ALVES are with the VDM Metals International GmbH, Kleffstraße 23, 58762 Altena, Germany. Contact e-mail: masood.hafez@acerinox.com J. SHARMA and N. BOZZOLO are with the MINES ParisTech, Centre de Mise en Forme des Matériaux (CEMEF), CNRS UMR 7635, PSL University, CS 10207, rue Claude Daunesse, 06904 Sophia Antipolis Cedex, France.
Manuscript submitted August 23, 2022; accepted February 20, 2023.



Published online: 21 March 2023

Table I. Nominal Chemical Compositions (Wt Pct) of Alloy 718 and VDM Alloy 780

| Alloy | Cr | Co | Mo | Nb | Fe | Al | Ti | C | Ni |
|---|---|---|---|---|---|---|---|---|---|
| Alloy 718 | 18.1 | — | 2.9 | 5.4 | 18.0 | 0.45 | 1.0 | 0.025 | bal |
| VDM Alloy 780 | 18.0 | 25.0 | 3.0 | 5.0 | < 3.0 | 2.0 | 0.3 | 0.025 | bal |

and sheets through complex production processes. The alloy being potentially suitable for a wide range of applications (and associated properties), grain size after forging needs to be precisely controlled, which is the underlying motivation of the present work.

The alloy development strategy of VDM Alloy 780 is based on the modification of the chemical composition of Alloy 718. The main differences between VDM Alloy 780 and Alloy 718 is the replacement of Fe by Co, higher Al content along with a lower Ti content in the former case to favor $\gamma'$ phase (Table I). This composition results in a microstructure consisting of the FCC-$\gamma$ matrix strengthened by nano-sized intermetallic precipitates of $Ni_3Al$ ($\gamma'$) and micrometric precipitates of $Ni_3Nb$-based ($\delta$) and $Ni_3Ti$-based ($\eta$) phases, which will be referred to as $\eta/\delta$ in the following,[2] for pinning grain boundaries and to help controlling the grain size during thermomechanical processing.[3–8]

Here, the focus is placed on the behavior of microstructure during and following the hot deformation process in single phase supersolvus domain to determine to what extent the grain size can be controlled during industrial forging in the absence of second phase particles to pin the grain boundaries. Dynamic and post dynamic recrystallization (DRX and PDRX, respectively) mechanisms and kinetics are studied based on laboratory hot compression tests and quantitative microstructure analyses. The earlier work published in Reference 9 is completed using a parametric study of the microstructure evolution allowing a better understanding of the influence of strain, strain rate, temperature and holding times on the grain sizes achieved in the VDM Alloy 780.

## II. EXPERIMENTAL METHODS

### A. *Material and Initial Microstructures*

VDM Alloy 780 is produced by triple melting, Vacuum Induction Melting (VIM)/Electro-Slag Remelting (ESR)/Vacuum Arc Remelting (VAR) and cogged into billet with a diameter of 156 mm over multiple forging heats. The samples for heat treatments and compression tests were taken out from the mid-radius of the billet.

The microstructure of the as-received billet material exhibited few Nb-rich carbide and Ti-rich nitride particles (zoomed in Figure 1(a) and arrowed in Figures 1(c) and (d)) along with presence of fine $\gamma'$ precipitates that are somewhat coarser at the grain boundaries (Figure 1(b)). Noteworthily, no $\eta/\delta$ phase particles were observed in the as-received billet state. The as-received billet material was partially recrystallized with an average grain size of 38 $\mu$m and involved residual stored energy as revealed by the contrast inside some of the grains, arrowed in the FSE image in Figure 1(c).

To study the recrystallization and grain growth kinetics in the single-phase domain without any bias induced by the residual stored energy present in the starting material, heat treatments at different temperatures used for the subsequent hot-compression experiments (1050 °C, 1080 °C and 1120 °C) were performed on the as-received billet material. All the three heat treatment temperatures are above the solvus temperatures of $\gamma'$ and $\eta/\delta$ phases (around 1000 °C). Holding time at each temperature has been adjusted to reach similar grains sizes, as shown in Table II. As the initial grain size also influences the recrystallization kinetics, the holding time at each temperature was adjusted to obtain grain sizes in a reasonable range (50 to 90 $\mu$m). A hold of 10 minutes at 1120 °C was required to ensure temperature homogeneity after introducing the sample between the compression tools, thus the annealing time could not be shortened more.

The three thermal treatments led to microstructures like the example shown in Figure 1(d), where the Forward Scattered Electron (FSE) intensities providing homogeneous color per grain indicate that the microstructure is free of the remnant stored energy. After thermal treatment (those of Table II), the carbide/nitride particles were still present but the $\gamma'$ phase was fully dissolved and did not form again during water quenching (Figure 1(e)). Except the presence of insoluble carbide and nitride particles, the heat treatment conditions in Table II thus generated single-phase microstructures free of stored energy, thus suitable for the forthcoming recrystallization kinetics study.

### B. *Hot Compression Tests*

Isothermal hot compression tests were performed using a MTS Landmark 370 device equipped with a radiative furnace. Temperature is controlled thanks to thermocouples placed in the tools close to the samples. Double-cone and cylindrical compression samples were machined from the mid-radius of the wrought billet (geometries presented in Figure 2) with the compression direction along billet axis.

The double cone geometry[10,11] offers the possibility to generate a range of plastic strain (0.4 to 1.3 with the employed geometry) along the radial direction of the sample. The cylinder geometry is used to obtain the flow curves from the compression tests when required in addition to the microstructure analyses (flow curves not shown here, being out of the scope of the paper). Compression tests on cylindrical samples have been performed up to different height reductions and corresponding local strain values at the center of the compressed samples (0.9, 1.3 or 1.7).

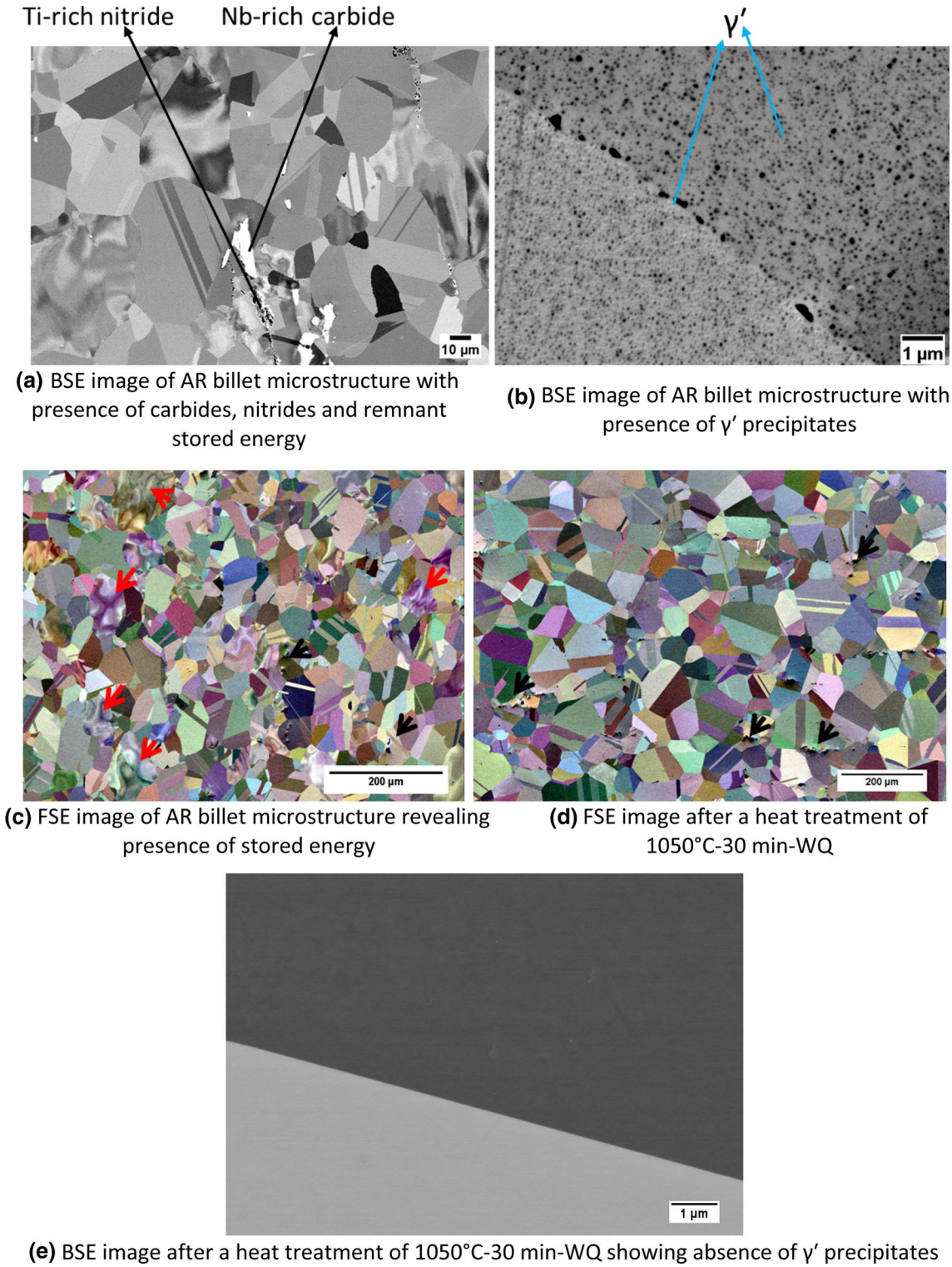


Fig. 1—(*a*) through (*c*) As-received (AR) billet material and (*d*, *e*) heat treatment at 1050 °C–30 min–WQ.

The applied thermomechanical conditions to investigate DRX and PDRX kinetics in VDM Alloy 780 is summarized in Figure 2. The thermomechanical parameters (temperature, strain, and strain rate) for the compression tests were chosen in line with the industrial practices of VDM Metals. The deformation tests were performed using two nominal strain rates, 0.01 and 0.1 $s^{-1}$, and three different temperatures (1050 °C, 1080 °C, and 1120 °C) following the holding times at each temperature given in Table II. The initial investigations suggested that the strain rate sensitivity in this alloy is weak and the impact of strain rate on

microstructural evolution weakens with temperature.[9] Therefore, the PDRX experiments on cylinder samples were performed at only 0.1 $s^{-1}$ (Figure 2(d)).

To study dynamic recrystallization kinetics, the samples were water quenched (WQ) as rapidly as possible after the end of deformation. In the current experimental set-up a quench delay of 1 to 3 seconds could not be avoided as the furnace has to be lifted out before the sample can be pushed into the quenching bath. Therefore, microstructures considered for the DRX kinetics are actually obtained after a short quench delay ranging from 1 to 3 seconds after deformation (measured after video recording). To study post-dynamic recrystallization, deformed samples were maintained inside the furnace of the compression testing machine for different holding times (6, 30 and 300 seconds) before water quenching.

**Table II. Heat Treatment Conditions Applied onto the As-Received Billet Material Before Compression to Obtain Single-Phase Microstructures (Without Second Phase Particles) and Without Stored Energy with Resulting Average Grain Sizes**

| Temperature, °C | Holding Time, min | Grain Size, $\mu$m |
|---|---|---|
| 1050 | 30 | 52 |
| 1080 | 15 | 66 |
| 1120 | 10 | 90 |

### C. *EBSD Analyses*

The compressed samples were cut through their diameter and polished for EBSD characterization using a Zeiss SUPRA40 Field Emission Gun Scanning Electron Microscope (FEG-SEM) equipped with a Bruker e-Flash detector. Microstructures were analyzed in the longitudinal section at three equidistant points along the radius of the double cone samples: center, one-third from the center and two-thirds from the center corresponding to local strain levels ($\varepsilon_{VM}$) of 1.3, 0.9 and 0.4 respectively. In case of cylinder samples, the microstructures were observed at the center at the three applied local strain levels: 0.9, 1.3 and 1.7. On all EBSD maps shown below, the compression direction is vertical.

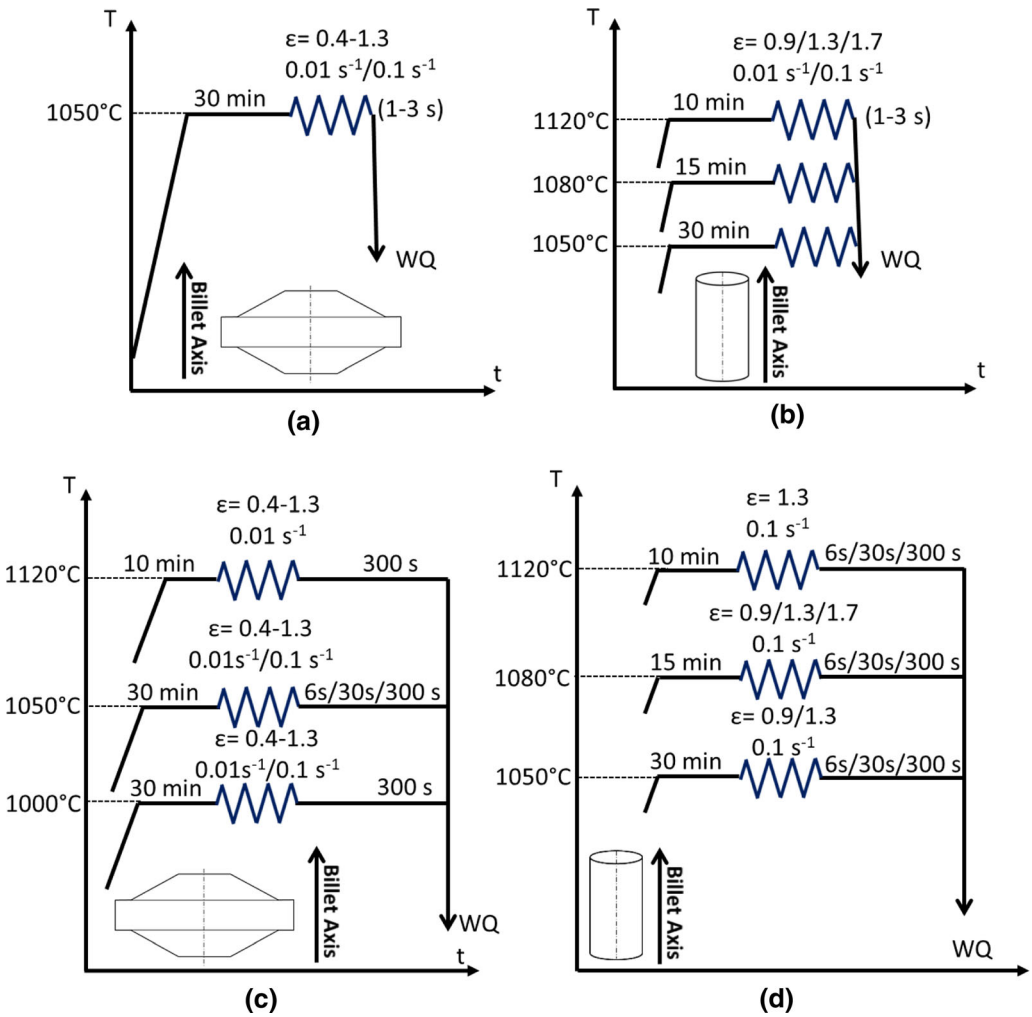


Fig. 2—Schematic representation of the applied thermomechanical conditions to study (*a*, *b*) DRX and (*c*, *d*) PDRX using double cone geometry and cylinder geometry.

An accelerating voltage of 20 keV was used at a working distance of 15 mm and maps were acquired with different step sizes varying from 0.19 to 0.63 $\mu$m on a region of 1200 × 900 $\mu$m. A minimum of around 2000 grains were taken into consideration for the calculation of grain size. A misorientation angle threshold of 10 deg was used to define a high angle grain boundary (HAGB) whereas a threshold of 5 to 10 deg was defined as a low angle grain boundary (LAGB) or a subgrain boundary. Twin boundaries were defined with a misorientation of 60 deg around ⟨111⟩111> axis with a tolerance of 7 deg. In the calculation of grain sizes, twin boundaries were considered as intragranular defects. The average grain size (defined as the mean equivalent circle diameter) was calculated by excluding grains smaller than a given value (2 to 3 $\mu$m) corresponding to the size of carbides/nitrides that were misindexed within the FCC structure in the raw EBSD maps.

As a result of plastic deformation, intragranular misorientations induced by the presence of dislocations can be quantified to semi-quantitatively estimate stored energy and to assess the extent of recrystallization using different parameters. The data obtained from EBSD analyses were post-processed using the open source MTEX toolbox in MATLAB.[12] The raw EBSD data were first filtered using the recently developed Local Linear Automatic Smoothing Splines method (LLASS).[13] This filter reduces the EBSD orientation noise that lies in the resolution of the classical EBSD (typical range of 0.5 to 1 deg) down to below 0.2 deg[13] and allows better recognition of recrystallized grains.[14]

Different parameters can be used to evaluate intragranular misorientations. In this study, Kernel Average Misorientation (KAM) maps were plotted to qualitatively visualize the extent of recrystallization and compare different microstructures within a given KAM scale. KAM is defined here as the average of the misorientation angles $\theta_{ij}$ between a given pixel $i$ and its $n$ neighbors $j$ as given by

$$\mathrm{KAM}_i = \frac{1}{n}\sum_{j=1}^{n}\theta_{ij} \qquad \square$$

The recrystallized grains were characterized by low KAM values and could thus be easily recognized on KAM maps. In the present case, as the initial grain sizes achieved after the thermal treatments of Table II were much larger than the recrystallized grains sizes obtained after hot deformation, the recrystallized fraction was calculated using a simple grain size threshold.

## III. RESULTS AND DISCUSSION

### A. *Dynamic Recrystallization*

Dynamic recrystallization (DRX) constitutes the formation and growth of the recrystallized grains during hot deformation. Like most nickel-based superalloys, VDM Alloy 780 is prone to necklace discontinuous DRX. Higher dislocation density at the grain boundaries lead to higher KAM values as visible in Figure 3(b), and in turn to the preferential nucleation of recrystallized grains at these locations of higher stored energy. A typical example of the resulting necklace-type structure observed after partial DRX during hot deformation is shown in Figure 3. This mechanism of recrystallization is well-reported for nickel-based superalloys, for example for Nimonic 80A from 950 °C to 1180 °C at 1 $s^{-1}$,[15] Alloy 625 from 900 °C to 1200 °C at 0.1 $s^{-1}$,[16] UNS N07208 nickel-based superalloy from 1060 °C to 1080 °C at 0.05 to 0.5 $s^{-1}$,[17] Alloy 718 from 920 °C to 1040 °C at 0.001 to 1 $s^{-1}$.[18,19]

The zoomed area of Figure 3(c) reveals that there are two types of recrystallized grains at the former grain boundaries: (i) few of them with intragranular misorientations arising from dynamic recrystallization, and (ii) others with much lower internal misorientations which are likely to have grown post-dynamically despite the quenching delay being as short as possible (1 to 3 seconds). The effect of post-dynamic evolution even with a quench delay of 3 seconds could thus not be completely avoided, which is consistent with the very fast PDRX kinetics reported earlier in the Alloy 718.[20,21] Noteworthily, as clearly visible on Figure 3, the necklace recrystallized grains exhibit quite a high twin density, which is a common feature for grains obtained after recrystallization.[22]

The influence of the thermomechanical parameters (temperature, strain and strain rate) on DRX kinetics are analyzed below.

#### 1. *Effect of strain*

The effect of the amount of plastic deformation on recrystallization can be understood by an increase in the number of potential nuclei as a result of stored energy getting to the critical level for nucleation at more and more locations in the microstructure, and of time available for these nuclei to form.[23]

Figure 4 presents the microstructural evolution at 1080 °C with increasing strain at 0.1 $s^{-1}$ With the increase in strain from 0.9 to 1.7, the recrystallized fraction ($F_r$) increases from 0.28 to 0.52. Recrystallization progresses by the appearance of new grains and the average size of the dynamically recrystallized grains ($D_r$) decreased slightly from 6.7 to 4.4 $\mu$m as the strain increased from 0.9 to 1.7. The recrystallized grain sizes are usually not highly affected by the applied strain level.[16,20,24,25]

The influence of strain on the recrystallized fraction is summarized in Figure 4(d) where recrystallized fraction increases with strain at a given temperature. However, it should be reminded that the initial grain size before deformation slightly differs at each temperature (Table II), which may affect the resulting recrystallized fractions through the density of grain boundaries available for nucleation. The DRX at 1120 °C remains faster even with a larger initial grain size before deformation which suggests that the influence of temperature is predominant over initial grain size in these experiments. Even at the highest temperature 1120 °C, a strain level as high as 1.7 was nevertheless still

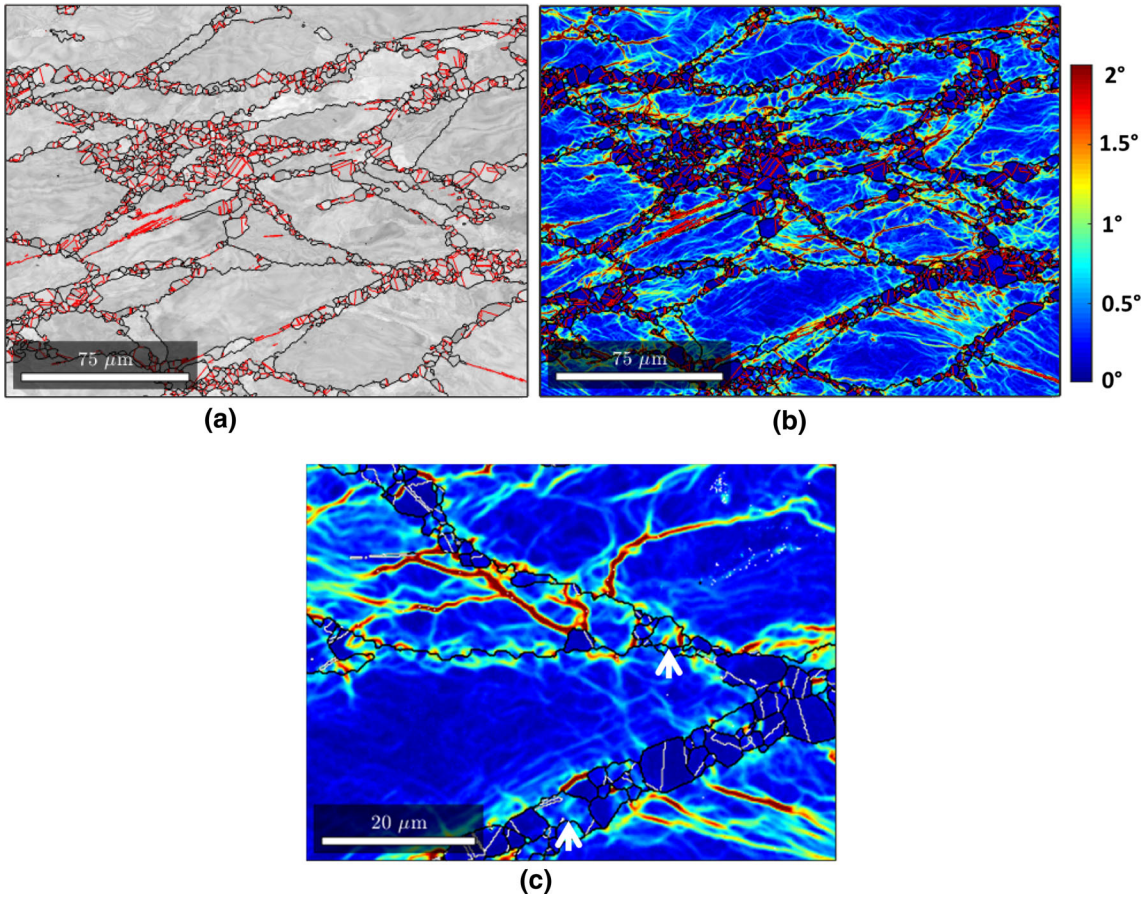


Fig. 3—Necklace-type structure observed after deformation at 1050 °C–0.1 $s^{-1}$–$\varepsilon$ = 0.9 with fast water quenching (< 3 s). (*a*) Band contrast image and (*b*) KAM map. Grain boundaries (> 10 deg) are plotted black. Twin boundaries (60 deg <111> with a tolerance of 7 deg) are plotted in red color in (a) and (b), in white in (*c*) (Color figure online).

insufficient to achieve full DRX (about 20 pct non-recrystallized left at 1.7 strain).

The DRX kinetics in the VDM Alloy 780 appear to be drastically slower than those of Alloy 718 investigated by Zouari *et al.*[19] At a strain rate of 0.1 $s^{-1}$, Alloy 718 is fully recrystallized dynamically after a strain of 1 at 1050 °C or 1.5 at 1080 °C, while the recrystallized fraction hardly reaches 25 and 50 pct in the VDM Alloy 780 for the same conditions respectively. When deformation is carried out at 1050 °C to a strain of 1.0 at lower rate, 0.01 $s^{-1}$, Alloy 718 is fully recrystallized whereas VDM Alloy 780 is not even 30 pct recrystallized.

The exact reason for the slower DRX kinetics would deserve being further studied. One assumption that can be raised is related to the high cobalt content. Cobalt is known to decrease the stacking fault energy in nickel-based superalloys.[26–28] Recovery mechanisms are disfavored by lower stacking fault energy values as dissociated dislocation climbing. In turn the formation of dislocation substructures, prefiguring the formation of recrystallization nuclei, is more difficult as stacking fault energy gets lower. This way the high cobalt content could play a role in the slow DRX kinetics in the VDM Alloy780. Noteworthily, the dynamically recrystallized fraction in Alloy 718Plus at 1025 °C was 48 pct for a strain of 0.8 while 59 pct for a strain of 1.2 using a strain rate of 0.01 $s^{-1}$.[29] The resulting recrystallized fractions in Alloy 718 Plus (9 wt pct cobalt) seem thus to be intermediate between the ones obtained in Alloy 718 (< 1 wt pct cobalt) and VDM Alloy 780 (25 wt pct cobalt) under similar deformation conditions. This is also in favor of assuming cobalt to be involved in the control of DRX kinetics.

Comparing the results of the present work with those published for the Alloy 718, it also turns out that the DRX grains sizes are different between both alloys. At a strain rate of 0.1 $s^{-1}$, the DRX grain size is 10 to 12 $\mu$m in the range at 1050 °C to 1080 °C in Alloy 718,[19] while it is about twice smaller in the VDM Alloy 780. This suggest that either the DRX grains grow slower, or they appeared later and had shorter time to grow in the case of VDM Alloy 780. A late appearance would be consistent with the assumption of a slow or difficult nucleation process evoked above. Nevertheless, a lower mobility of the recrystallization front cannot be excluded from these few observations and both effects could possibly be at play together.

2. *Effect of strain rate*

Higher strain rate increases the dislocation density and consequently potential sites for nucleation of recrystallized grains. However, shorter deformation time

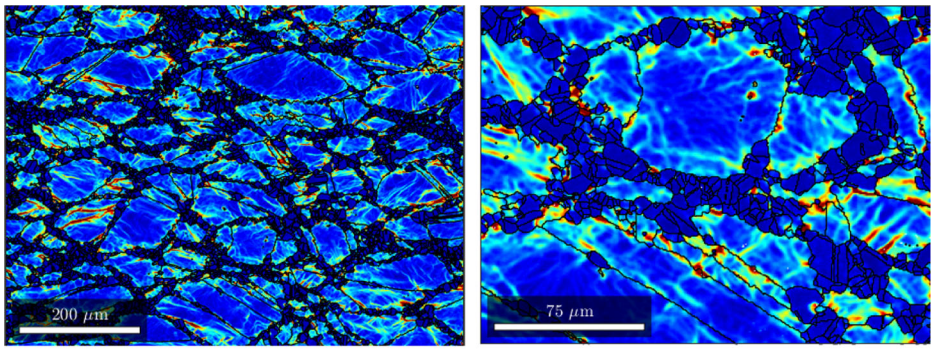


**(a)** ε = 0.9; $F_r$ = 0.28; $D_r$ = 6.7 μm

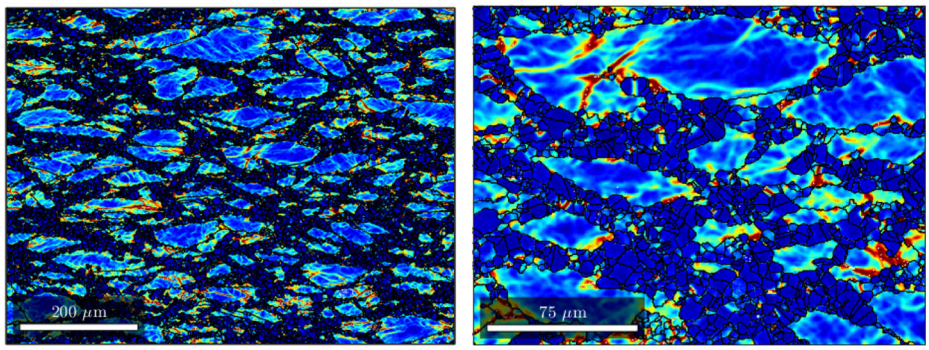


**(b)** ε = 1.3; $F_r$ = 0.47; $D_r$ = 5.4 μm

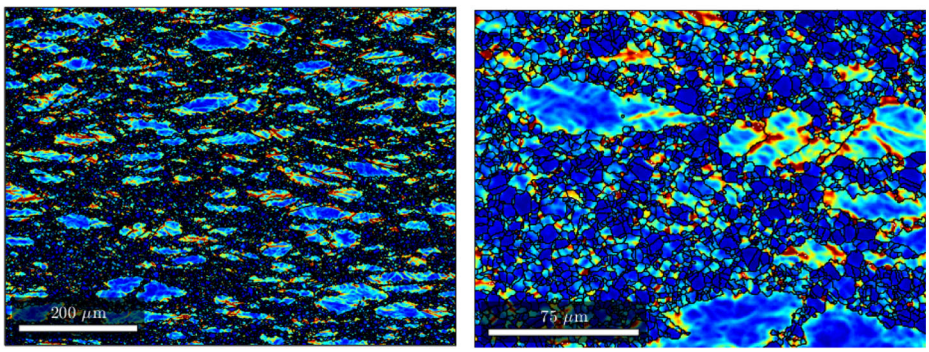


**(c)** ε = 1.7; $F_r$ = 0.52; $D_r$ = 4.4 μm

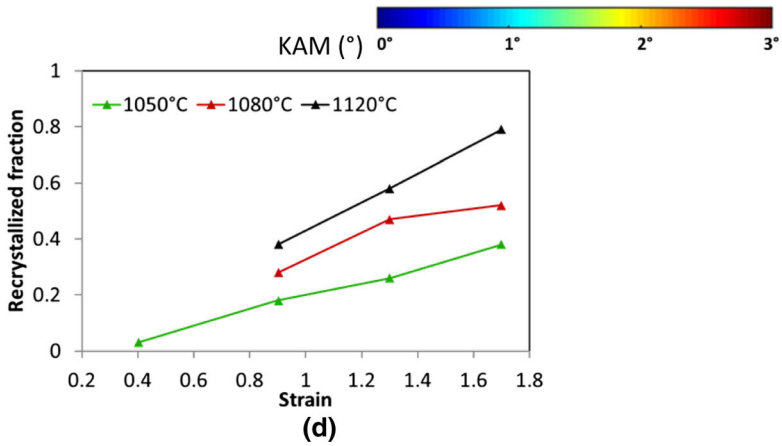


**(d)**

Fig. 4—(*a*) through (*c*) KAM maps at different strain levels ($\varepsilon$) at 1080 °C–0.1 $s^{-1}$–QD = 1 to 2 s and (*d*) evolution of dynamically recrystallized fraction with strain at different temperatures at 0.1 $s^{-1}$. Grain boundaries (> 10 deg) and twin boundaries are plotted black. The recrystallized fraction and recrystallized grain sizes are mentioned at each strain level. A zoomed KAM map is provided for each condition.

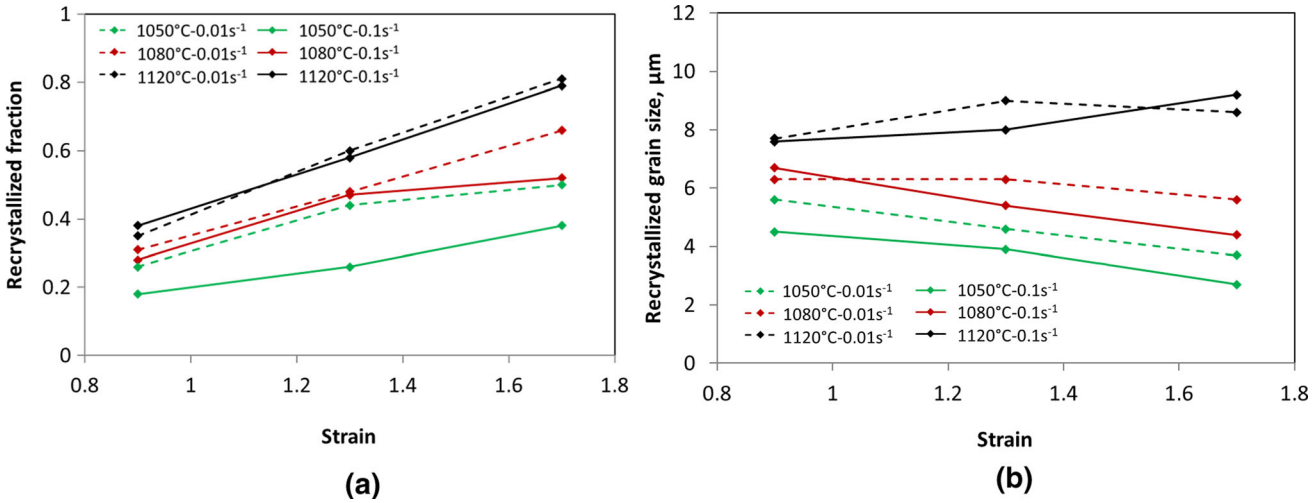


Fig. 5—Influence of strain rate on (*a*) recrystallized fraction and (*b*) average recrystallized grain size at different strain levels and temperatures.

available with higher strain rates limits both the number of formed nuclei and the extent of their growth as recrystallized grains, thus lowering the recrystallisation kinetics (as described in a strain scale).[18] Conversely, a longer time available for the microstructure to evolve at lower strain rates can lead to an early onset of DRX (*i.e.*, at a lower strain value).[17] Such a decrease in dynamic recrystallization kinetics with increasing strain rate is a common observation and has been reported in many different alloys.[21,30–40]

The influence of strain rate on the recrystallized fraction experimentally obtained in this work is summarized in Figure 5(a). Indeed, at a given strain level, lower strain rate (0.01 $s^{-1}$) results in higher recrystallized fraction. However, this effect is less pronounced as the temperature increases from 1050 °C to 1120 °C. At higher temperatures, the sensitivity of recrystallization kinetics to strain rate becomes much weaker.

The effect of strain rate on the recrystallized grain sizes is presented in Figure 5(b). For a strain of 0.9 at 1050 °C, the DRX grain size increased from 4.5 $\mu$m at 0.1 $s^{-1}$ to 5.6 $\mu$m at 0.01 $s^{-1}$. The higher strain rate generates comparatively finer DRX grains. At higher strain rates, the higher nucleation density, and less time available for grain boundary migration can limit the growth of recrystallized grains.[25,33] On the other hand, due to lower dislocation density, the driving force for the migration of the recrystallization front is lesser at low strain rates. Nevertheless, it is interesting to note that the DRX grain sizes do not differ significantly between the two applied strain rates.

This is contrary to Alloy 718 where the dynamically recrystallized grain sizes were significantly affected by the applied strain rates.[19] The DRX grain size was around 10 $\mu$m at 0.1 $s^{-1}$ and 20 $\mu$m at 0.01 $s^{-1}$ when the samples were deformed to a strain of close to 1.1 at 1050 °C.[19] It must also be noted that at higher strain rates, self-heating may play a significant role and post-dynamic recrystallization can affect the measured recrystallized fraction even with quenching delays as short as 2 to 3 seconds.[21,33] The tendency for a slight decrease in the DRX grain sizes with increasing strain rate in Figure 5(b) could be explained by the impingement of the recrystallized grains owing to higher nucleation density or to late nucleation and thus less time to grow.

3. *Effect of temperature*

A rise in temperature increases the grain boundary mobility and thus should accelerate the growth of the recrystallized grains. Conversely, higher temperatures promote dynamic recovery which reduces the dislocation density and hence lowers the driving force for the migration of the recrystallization front. Regarding nucleation, the effect of temperature is not trivial either since the decrease in dislocation density and recrystallization driving force should lead to lower nucleation density, but on the other hand the formation of nuclei proceeds by local arrangement of defects or recovery mechanisms which are promoted by higher temperatures. Figures 6(a) through (c) shows that the recrystallized fraction increases with temperature at a given strain and strain rate. The recrystallized fraction achieved upon a strain of 1.3 and 0.1 $s^{-1}$ increases from 0.26 at 1050 °C to almost 0.6 at 1120 °C.

At a given strain and strain rate, temperature was found to have a favorable influence on recrystallization as illustrated in Figure 6(d). Grain sizes increased also with temperature for all the strain levels in Figure 6(e). On the contrary, the number of recrystallized grains per unit area decreased as temperature increased (Figure 6(f)). This indicates that the higher recrystallized fraction at higher temperature results from growth of recrystallized grains and is not linked to an increase in the density of nuclei.

## B. *Post-dynamic Recrystallization*

Once deformation is completed, the material can still experience high temperatures that lead to metallurgical phenomena such as static recovery, recrystallization, grain growth, and even precipitation while cooling. Such

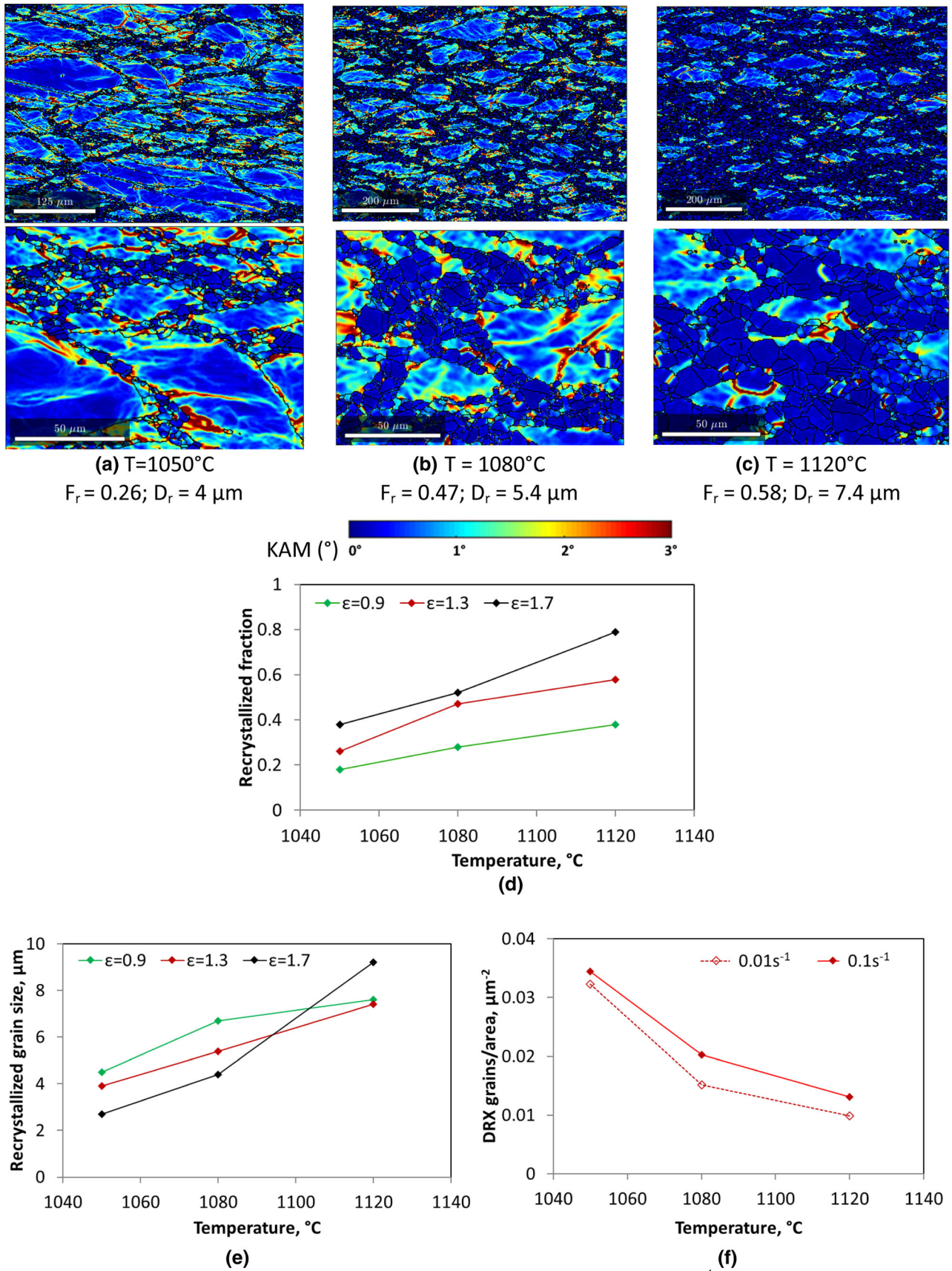


Fig. 6—(*a*) through (*c*) KAM maps showing the effect of temperature on DRX at $\varepsilon = 1.3$ and $\dot{\varepsilon} = 0.1\ s^{-1}$, (*d*) Recrystallized fraction at $0.1\ s^{-1}$, (*e*) DRX grain sizes for different strains at $0.1\ s^{-1}$, and (*f*) Number of recrystallized grains per unit area for the two applied strain rates at $\varepsilon = 1.3$. Grain boundaries (> 10 deg) and twin boundaries are plotted black. The recrystallized fraction and recrystallized grain sizes are mentioned at each temperature. A zoomed KAM map is provided for each condition.

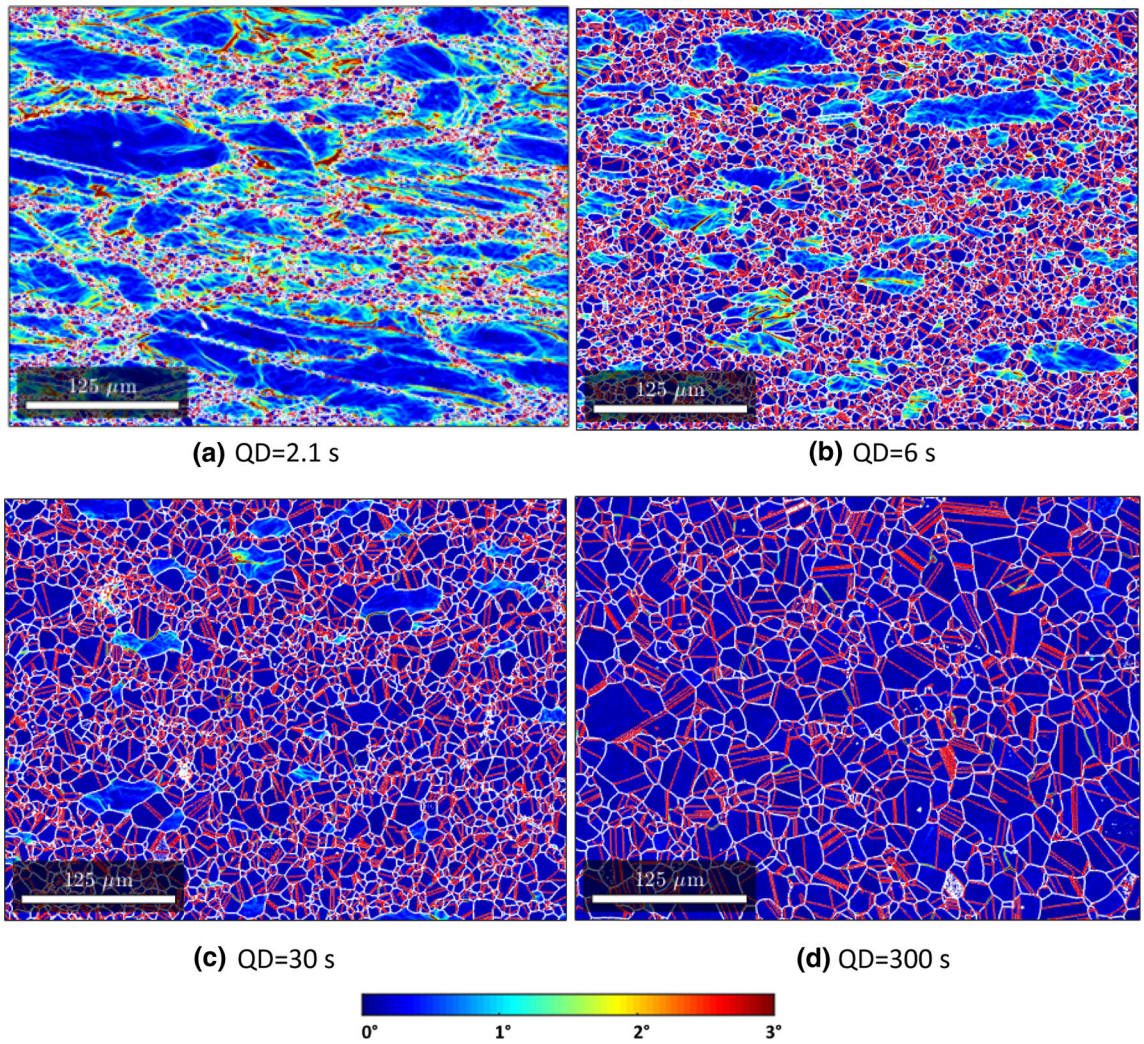


Fig. 7—KAM maps showing post-dynamic evolution at 1050 °C–$\dot{\varepsilon}$ = 0.1 $s^{-1}$–$\varepsilon$ = 1.3 as a function of holding time; (*a*) shortly after deformation, after (*b*) 6 s, (*c*) 30 s and (*d*) 300 s. Grain boundaries (> 10 deg) are plotted white. Twin boundaries (60 deg ⟨111⟩ with a tolerance of 7 deg) are plotted red (Color figure online).

post-dynamic evolution is usually always present in industrial forging processes due to the slow cooling of the large industrial parts. In addition, transfer of the part between successive processing steps also involves post-dynamic evolution.

The dynamically recrystallized microstructure is heterogeneous and consists of (a) freshly formed small dynamically recrystallized nuclei and grains which are almost dislocation free, (b) larger recrystallized grains with higher dislocation content which have grown during deformation, and (c) deformed grains with much higher dislocation density.[41] The main driving force for PDRX is the consumption of stored energy present in the non-recrystallized matrix and in the work hardened DRX grains by the growth of the DRX nuclei and grains with low dislocation density. Such development of pre-existing DRX grains or nuclei is referred to as meta-dynamic recrystallization. If the latter is not too fast, static nucleation may also occur concomitantly, so that post-dynamic recrystallization can results from a combination of metadynamic and static recrystallization phenomena. In practice discriminating PDRX grains arising from either metadynamic or static recrystallization is not feasible since both types of grains have low intragranular misorientations.

The influence of different parameters on the microstructure evolution during the PDRX process is discussed below, based on experiments with post-deformation isothermal holding times.

1. *Effect of post-deformation holding time*

The samples after deformation were kept at the deformation temperatures for different holding times or quench delays (QD). The post-dynamic evolution was found to be rapid, especially at the beginning, owing to the high amount of stored energy present in the microstructure at the end of deformation. Post-dynamic microstructural evolution is illustrated on Figure 7 at a strain of 1.3 applied at 1050 °C and 0.1 $s^{-1}$. Figure 8 shows the corresponding grain size and recrystallized

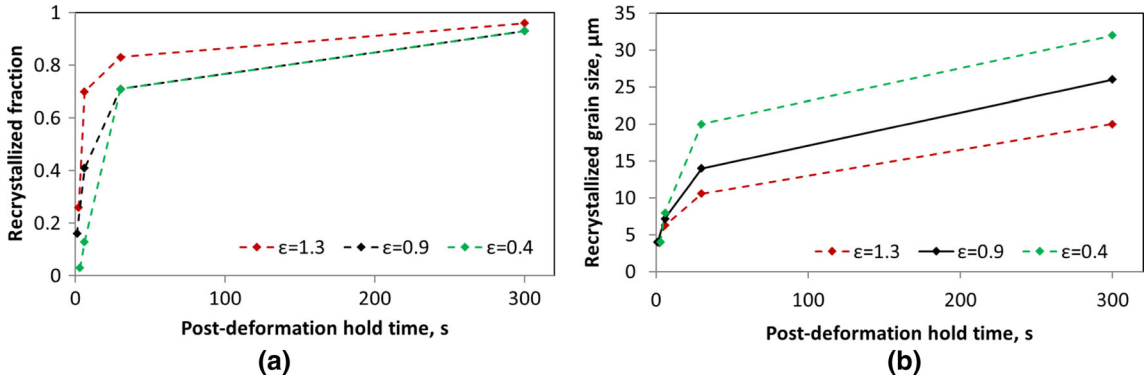


Fig. 8—Evolution of (*a*) recrystallized fraction and (*b*) grain size with post-deformation holding time for different strain levels at 1050 °C and 0.1 $s^{-1}$ (Color figure online).

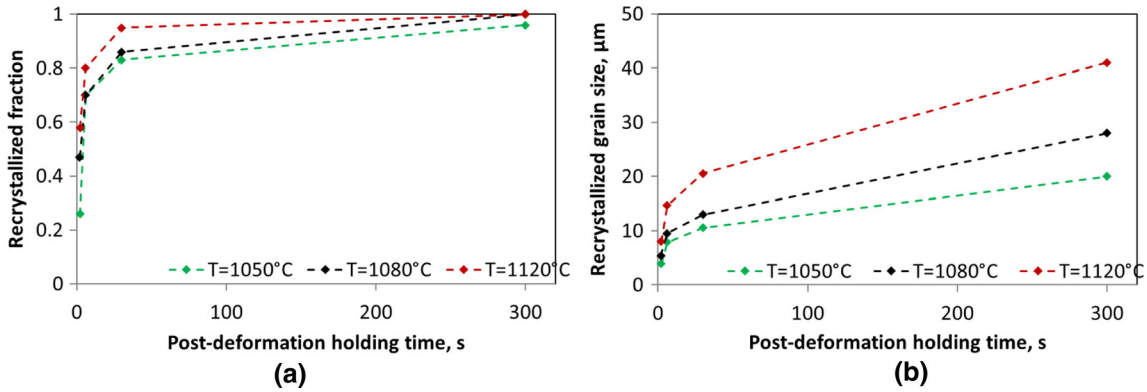


Fig. 9—Evolution of (*a*) recrystallized fraction and (*b*) recrystallized grain size with post-deformation holding time for different temperatures at $\varepsilon = 1.3$ and 0.1 $s^{-1}$.

fraction evolutions, in red, as well as the results obtained when varying strain level.

Although the dynamically recrystallized fractions are different at each strain level (Figure 6), all microstructures were almost completely recrystallized after 5 minutes of post-deformation hold, with significant changes already in a first few seconds (Figures 7(b) and 8(a)).

The recrystallized grains grow as the quench delay increases (Figure 8(b)); for each strain level, recrystallized grain size increased with post-deformation holding time. During early stages of PDRX, the recrystallized grain sizes increase from 4 $\mu$m after 2 seconds to almost twice after 6 seconds and to 11 $\mu$m after 30 seconds of post-deformation hold at $\varepsilon = 1.3$ (Figures 7(b) and 8(a)). However, towards the later stages of PDRX, from 30 seconds to 5 minutes, the growth kinetics slowed down, and recrystallized grain sizes increased from 11 to 20 $\mu$m. The final microstructure appears to be quite uniform in terms of grain sizes in Figure 7(d) compared to the situation right after deformation (Figure 7(a)).

Similar analysis has been conducted at 1080 °C and 1120 °C at a constant strain level (1.3) and a strain rate of 0.1 $s^{-1}$. The evolution of recrystallized fraction and recrystallized grain sizes are shown in Figure 9. The same trends as on Figure 8 are retrieved again: kinetics are faster in the early stages of the post-dynamic regime, when stored energy is at play (at the three deformation temperatures, microstructures are already around 70 pct recrystallized with only 6 seconds of post-deformation hold), and the recrystallized grain sizes increase with both temperature and post-deformation holding time (Figure 9(b)).

At the beginning of post-dynamic evolution, the growth of recrystallized grains is primarily controlled by the presence of stored energy in the microstructure. However, the recrystallized grains impinge each other as they get into contact and at this stage the grain size mostly depends on the density of the recrystallized grains. Beyond that, after stored energy has been fully consumed, the material enters the so-called grain growth regime, that is driven by capillarity forces. The thermodynamic driving force for capillarity driven grain growth is the reduction of grain boundary energy, which is much lower than that of recrystallization.[41] The driving pressures due to stored energy and to grain boundary curvature are indeed in the order of 2 to 20 and $10^{-2}$ MPa, respectively.[41] This implies that the grain boundary migration under capillarity is much slower as compared to that during recrystallization, which explains why the increase in grain size slows down in the late stages of the post-dynamic regime.

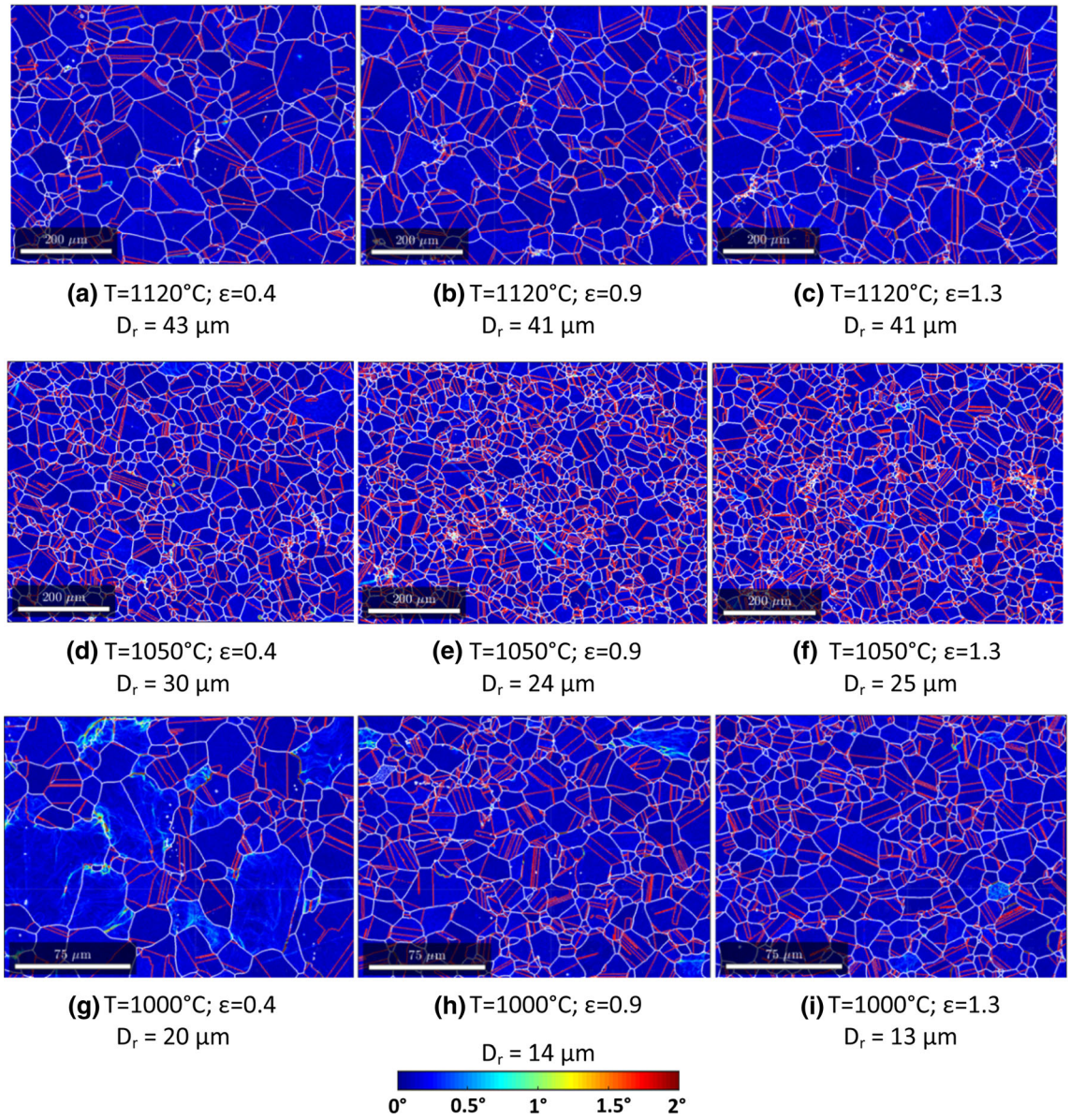


Fig. 10—KAM maps showing the effect of strain levels on PDRX for different temperatures at $\dot{\varepsilon} = 0.01\ s^{-1}$–QD = 5 minutes. Grain boundaries (> 10 deg) are plotted white and twin boundaries (60 deg ⟨111⟩ with a tolerance of 7 deg) are plotted red. Strain level increasing from left to right and temperature increasing from bottom to top. The recrystallized grain size is provided for each condition (Color figure online).

2. *Effect of prior strain level and of strain rate*

Here the influence of strain level and strain rate on the resulting microstructure following PDRX is considered for a constant hold time of 5 minutes in Figure 10. It appears that at 1120 °C or 1050 °C, the microstructure obtained after 5 minutes isothermal hold is not significantly affected by the amount of prior deformation (Figures 10(a) through (c) and (d) through (f) respectively). Only the sample deformed at 1000 °C to 0.4 strain was not fully recrystallized after 5 minutes isothermal hold (Figure 10(g)). However, for higher strain levels at 1000 °C ($\varepsilon = 0.9$ or 1.3), the microstructure was almost fully recrystallized with a smaller recrystallized mean grain size (around 13 $\mu$m) than at the other two temperatures.

The evolution of DRX and PDRX fractions as a function of strain is plotted in Figure 11(a) for the two strain rates and different holding times at 1050 °C. Here, the DRX fractions obtained with the shortest quench delay are marked as DRX. It is worth noting that, at this temperature, despite the different initial DRX fractions for the two strain rates, recrystallization is completed for all deformation conditions with a quench delay of 5 minutes including for the lowest applied strain level (0.4). The recrystallized grain sizes plotted in Figure 11(b) do not differ significantly for the two strain rates. With the progress of PDRX, the effect of deformation (strain and strain rate) on the microstructural evolution becomes secondary. The final microstructure appears to be mainly controlled by

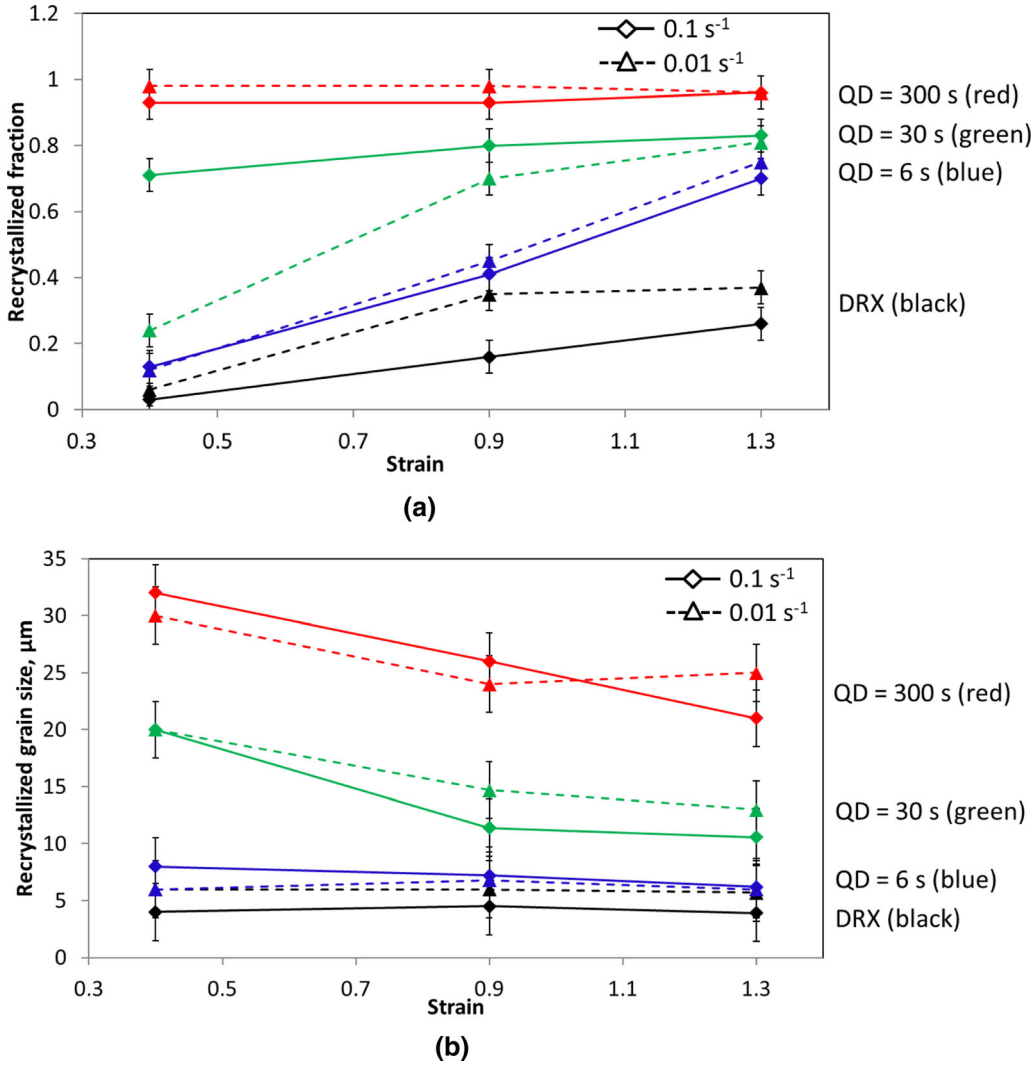


Fig. 11—Evolution of (*a*) recrystallized fraction and (*b*) grain size as a function of strain for two applied strain rates at 1050 °C.

temperature. Similar observations were found in case of another nickel-based superalloy (UNS N07208) where the post-dynamic evolution was found to be weakly coupled to the prior deformation steps and primarily dependent on temperature.[17] Such a behavior is an asset from industrial point of view as the strain level is never uniform in a forged piece, and therefore the DRX microstructure can be quite heterogeneous throughout the piece. Some time left at high temperature after forging to let PDRX proceed allows for microstructure homogenization.

Figure 12 shows the microstructures obtained after deformation at $\dot{\varepsilon} = 0.1\ s^{-1}$ up to $\varepsilon = 1.3$ and with 5 minutes hold at the three temperatures. Grain size increased from 20 $\mu$m at 1050 °C to 41 $\mu$m at 1120 °C.

As discussed in Section III–A the DRX kinetics of VDM Alloy 780 are relatively slow, slower than those of Alloy 718, but the PDRX kinetics are shown here to be quite fast, comparable to those of Alloy 718 based on the data of Reference 19. On the other hand, the recrystallized grain size in Alloy 718 increased post-dynamically from 10 to 50 $\mu$m in 5 minutes at 1050 °C.[19] For VDM Alloy 780, the grain sizes grew from 4 to around 32 $\mu$m at this same temperature. This suggests that the final recrystallized grains generated after the end of the forging process would be finer in the case of VDM Alloy 780.

### C. *Critical Strain to Achieve Full Recrystallization*

A fully recrystallized microstructure and homogenous grain sizes at the end of forging operations are crucial with regards to the industrial requirements. Section III–A revealed that the DRX kinetics in VDM Alloy 780 is slow, which could make recrystallization achievement difficult in low strain areas. However, the fast post-dynamic evolution can compensate for this slow DRX kinetics. The question addressed in this section is to determine what is the strain threshold (and related DRX fraction) below which the microstructure would not recrystallize post-dynamically.

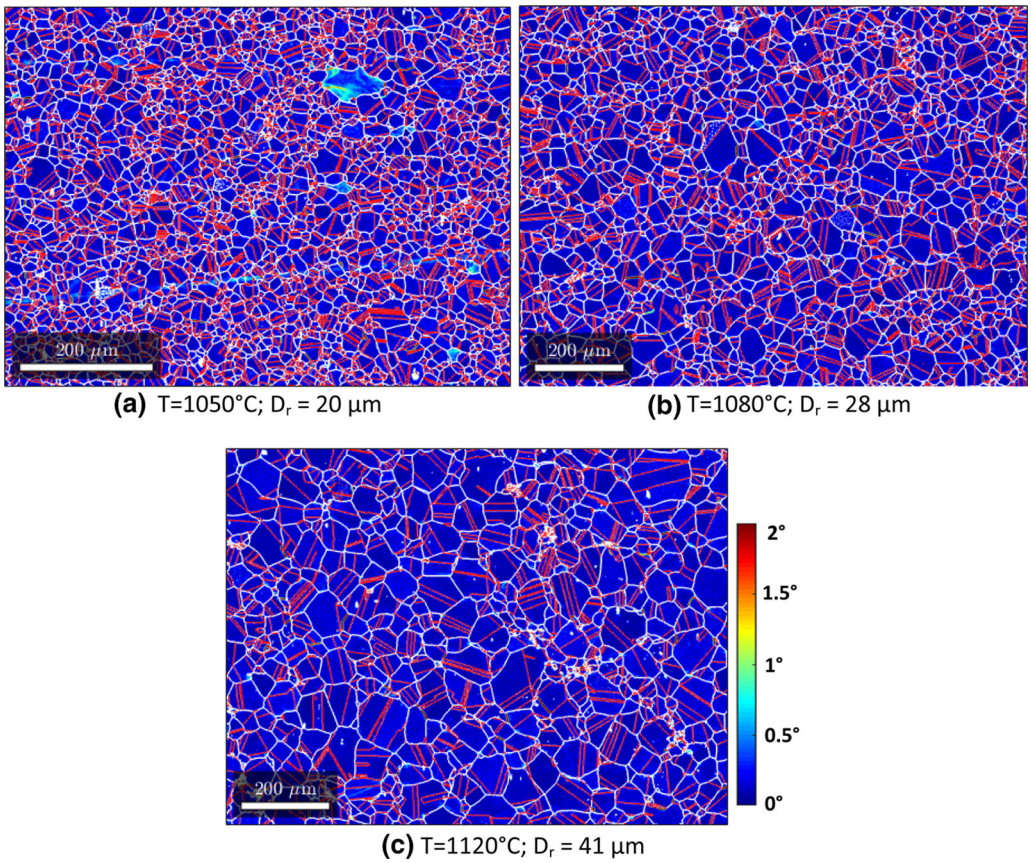


Fig. 12—KAM maps showing the effect of temperature on PDRX microstructures at $\dot{\varepsilon} = 0.1\ s^{-1}$–$\varepsilon = 1.3$–QD = 5 minutes. Grain boundaries (> 10 deg) are plotted white. Twin boundaries (60 deg ⟨111⟩ with a tolerance of 7 deg) are plotted red. The recrystallized grain sizes are mentioned at each temperature (Color figure online).

Critical conditions to achieve complete recrystallization were investigated using a low strain double cone geometry sample (where the local strain varies from 0.08 to 0.36).[10] The sample was first heated and held for 30 minutes at a deformation temperature of 1050 °C followed by deformation at a strain rate of 0.1 $s^{-1}$. A post-deformation hold of 5 minutes was first applied before the sample was water quenched. The microstructures at different strain levels are shown in Figure 13. It can be noted that a strain of 0.36 and even 0.2 are sufficient to obtain an almost fully recrystallized microstructure with 5 minutes of post-deformation hold. However, the microstructure when the strain level is around 0.08 is not fully recrystallized and involves large non-recrystallized grains (shown by arrows in Figure 13(a). The same sample was then heat treated at 1050 °C for 30 minutes, followed by water quenching, to check whether the low strain areas would recrystallize further with longer hold.

Following this additional heat treatment, the microstructures were found to be completely recrystallized for all the strain levels (Figures 13(d) through (f)), including the lowest one of 0.08. The recrystallized grain sizes obtained after 30 minutes of hold were close to 60 $\mu$m and were found to be similar at the three strains. During isothermal annealing, the recrystallized grains observed after 5 minutes of post-deformation holding time at the low strain end of the sample, in Figure 13(a), grew to complete the recrystallization, while already recrystallized areas at high strain levels underwent capillarity driven grain growth. Quite surprisingly, both these mechanisms—of recrystallization completion at the low strain end of the sample and of grain growth at the other end led to a uniform grain size after 30 minutes cumulated time at 1050 °C after deformation. This opens another perspective to this work which would aim at determining whether the same grain size would been obtained at other temperatures and then why, or if it is just fortuitous at the temperature used here, 1050 °C.

It is worth pointing out that low strain regions have been many times reported to be prone to the development of bimodal grain size distributions after thermal treatment in nickel-based superalloys. At low deformation conditions such as $\varepsilon = 0.02$, isolated grains of 700 $\mu$m in size were observed in René 88DT nickel-based superalloy after compression at room temperature followed by a solutionizing treatment of 60 seconds at 1150 °C.[42] In Alloy 718 processed at subsolvus temperature, selective growth of few grains consisting of fine grains of 6.2 $\mu$m along with one overgrown grain population of 47 $\mu$m was observed when the samples were deformed at 985 °C to a strain of

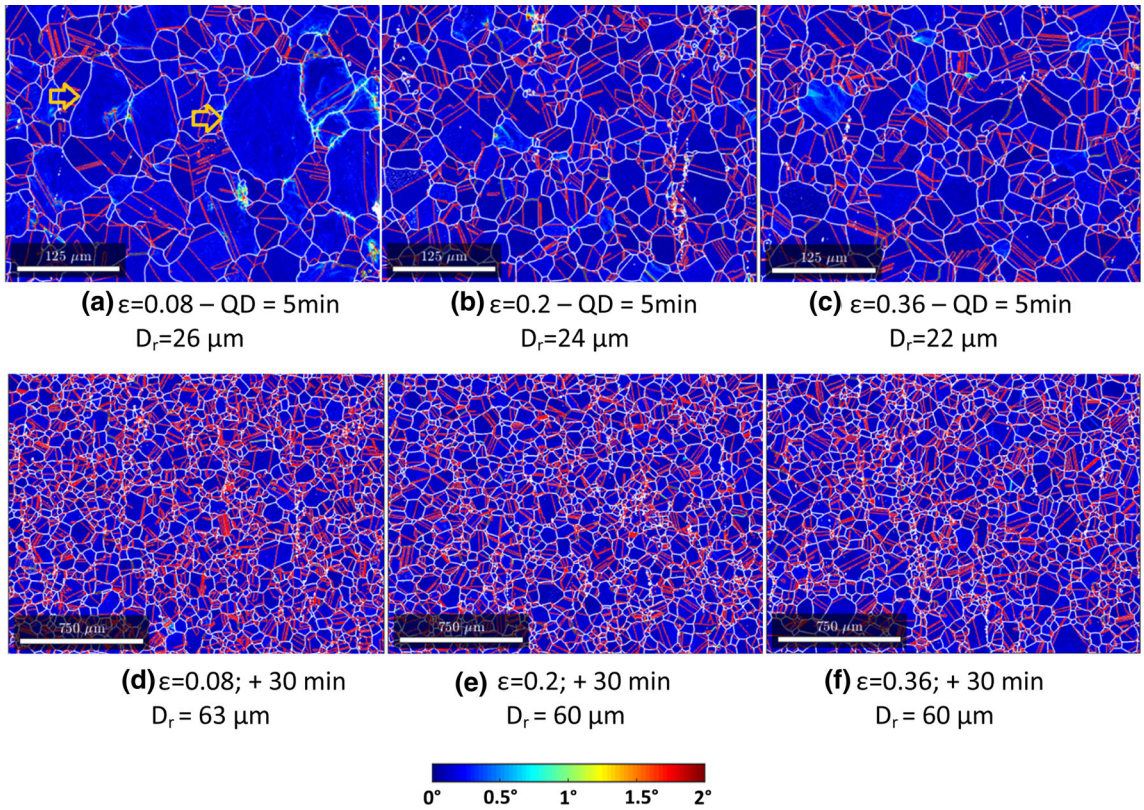


Fig. 13—(*a* through *c*) Microstructures obtained after hot-compression to different strain levels (0.08, 0.2, 0.36, respectively) at 1050 °C to 0.1 $s^{-1}$ with 5 minutes hold after the end of deformation followed by water quenching and (*d* through *f*) Same samples after additional heat treatment for 30 minutes at 1050 °C. KAM maps with overlaid grain boundaries (> 10 deg) plotted white and twin boundaries (60 deg ⟨111⟩ with a tolerance of 7 deg) plotted red. Recrystallized grains sizes are provided under each map (Color figure online).

0.1 followed by an annealing at 985 °C for 2 hours.[43] Recrystallization at low strain levels can result in limited nuclei density for static recrystallization due to low stored energy. These nuclei and recrystallized grains once formed grow and consume the available stored energy of the deformed grains.[10] This leads to larger grains during annealing due to the limited number of nuclei impinging each other. Sometimes, deformation close to critical conditions can lead to selective growth of few grains over others leading to a heterogeneous microstructure in terms of grain sizes.[10] This phenomenon is referred using different terminologies such as abnormal grain growth, critical grain growth, inhomogeneous grain growth, secondary recrystallization.[44–47]

However, in VDM Alloy 780 such phenomenon leading to heterogeneous grain sizes was not observed down to a strain value of 0.08. The microstructures evolved similarly irrespective of the amount of deformation once recrystallization is completed (Figure 13). The final grain sizes after the isothermal hold at 1050 °C for 30 minutes) are similar in the strain range from 0.08 to 0.36. This is another important characteristic of VDM Alloy 780 from an industrial point of view. This study revealed that a hold of 30 minutes at 1050 °C after deformation could generate homogenous and fully recrystallized microstructures for a strain as low as 0.08.

### D. *Tentative to Extend Single Phase Domain Below the ($\eta/\delta$ and $\gamma'$) Solvus Temperature*

To further refine the recrystallized grain sizes (compared to Sections III–A and III–B), attempts were made to extend the singe-phase domain to lower temperatures (below the solvus temperature of $\eta/\delta$ and $\gamma'$ phases).

When the as-received billet sample was held at 980 °C (below solvus temperature of $\eta/\delta$ and $\gamma'$ phases), for 1 hour followed by water quenching (Figure 14(a)), spherical $\gamma'$ precipitates are indeed observed in addition to a few $\eta/\delta$ particles (Figure 14(c)). However, when the billet sample was first solutionized at 1050 °C–15 minutes followed by a holding of 1 hour at 980 °C (Figure 14(b)), the microstructure was free of second phase particles after quenching as shown in Figure 14(d). This suggests that the precipitation kinetics is slowed down in the latter case even though 980 °C is below the solvus temperature of $\eta/\delta$ and $\gamma'$ phases. This treatment results in an average grain size of about 44 $\mu$m.

To study dynamic recrystallization, a double-cone billet sample was first continuously cooled from 1050 °C to 980 °C followed by a hold of 15 minutes at 980 °C before undergoing deformation. The microstructure after such thermal path (Figure 15(a)) is free of $\gamma'$ and $\eta/\delta$ phase particles (Figure 15(b)). Deformation was then performed to a strain of 1.3 using a strain rate of 0.1 $s^{-1}$ followed by water quenching as schematized in

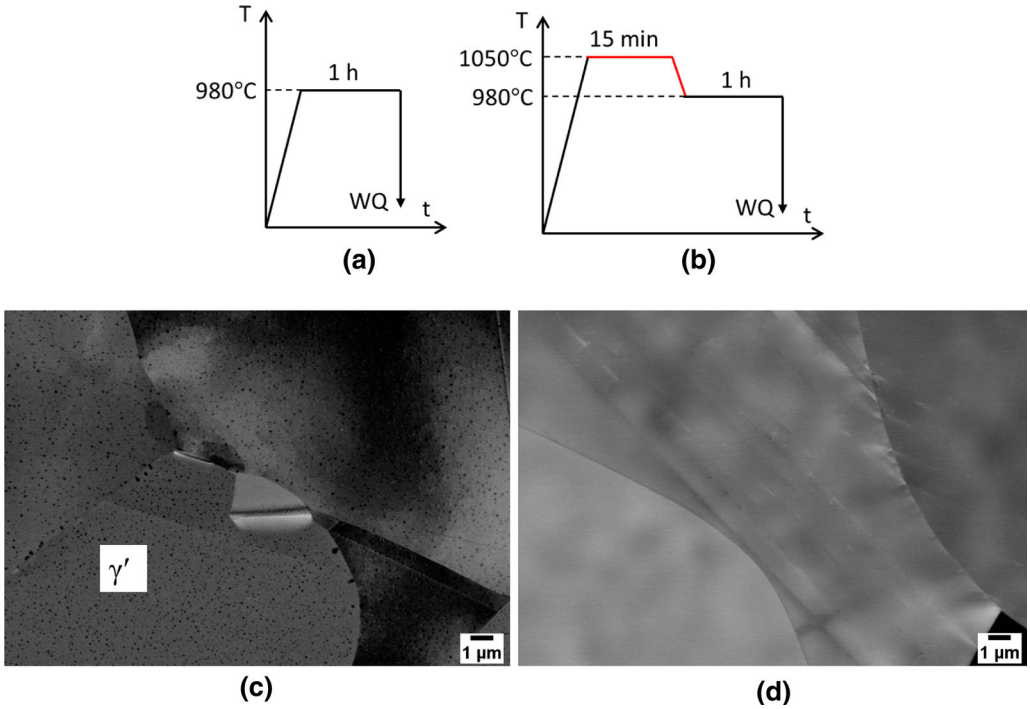


Fig. 14—Effect of thermal path on $\gamma'$ precipitation in billet samples. (*a*) Isothermal heat treatment at 980 °C–1 h–WQ and (*b*) supersolvus treatment of 1050 °C–15 minutes followed by furnace cooling to 980 °C and subsequent holding of 1 h before water quenching. Micrographs (*c*) and (*d*) show the microstructure following the heat treatments (a) and (b), respectively.

**Table III. Initial Grains Sizes and Heat Treatment Conditions Applied for Establishing Grain Growth Kinetics**

| *T*, °C | Billet, $\mu$m | Holding Time | PDRX, $\mu$m | Holding Time |
|---|---|---|---|---|
| 1050 | 44 | 15 min, 30 min, 1 h, 2 h | 22 | 15 min, 30 min, 1 h, 2 h |
| 1080 | 66 | 15 min, 30 min, 1 h, 2 h | 28 | 15 min, 1 h |
| 1120 | 90 | 15 min, 30 min, 1 h, 2 h | 39 | 15 min, 30 min, 1 h |

Figure 15(c). Formation of new recrystallized grains of about 1 to 2 $\mu$m with the typical necklace morphology is seen in Figure 15(d). Precipitation of fine $\gamma'$ precipitates could not be avoided despite fast quenching (QD = 1.3 s), mainly in the non-recrystallized grains (red arrows in Figure 15(e)). Interestingly, $\eta/\delta$ phase was not observed under these conditions indicating their slow precipitation kinetics.

The evolution of $\gamma'$ could be clearly seen after a post-deformation holding time of 5 minutes in Figure 15(f). In this case, $\gamma'$ precipitates are seen throughout the deformed matrix where the dislocation density is relatively higher as compared to the recrystallized grains. This kind of rapid precipitation of $\gamma'$ in the non-recrystallized grains as compared to the recrystallized grains was also observed in AD730.[48] Dislocations can accelerate nucleation events by providing faster diffusivity paths for the precipitate forming elements[49,50] and may also help nucleation by relaxing the elastic strains associated with the formation of precipitates.[48] Therefore, the results in Figure 15 demonstrated that the single-phase domain cannot be extended to 980 °C in VDM Alloy 780 due to fast dynamic precipitation of $\gamma'$ particles.

Despite the slow $\gamma'$ phase precipitation kinetics observed under static conditions in the VDM Alloy 780, the experiments reported in this section shown that precipitation is drastically accelerated dynamically and in turn strongly hinders recrystallization. In a supersolvus industrial forging route, one should thus avoid local cooling of the forged piece below the solvus temperature, as $\gamma'$ phase precipitation is shown here to be onset within few seconds of hot deformation and then to be detrimental for recrystallization.

### E. *Grain Growth Kinetics*

Grain growth kinetics, meaning capillarity driven grain growth, in VDM Alloy 780 were determined using a series of isothermal heat treatments. The capillarity-driven grain growth was established in the temperature range of 1050 °C to 1120 °C using (i) as-received billet samples after a heat treatment of 15 minutes at

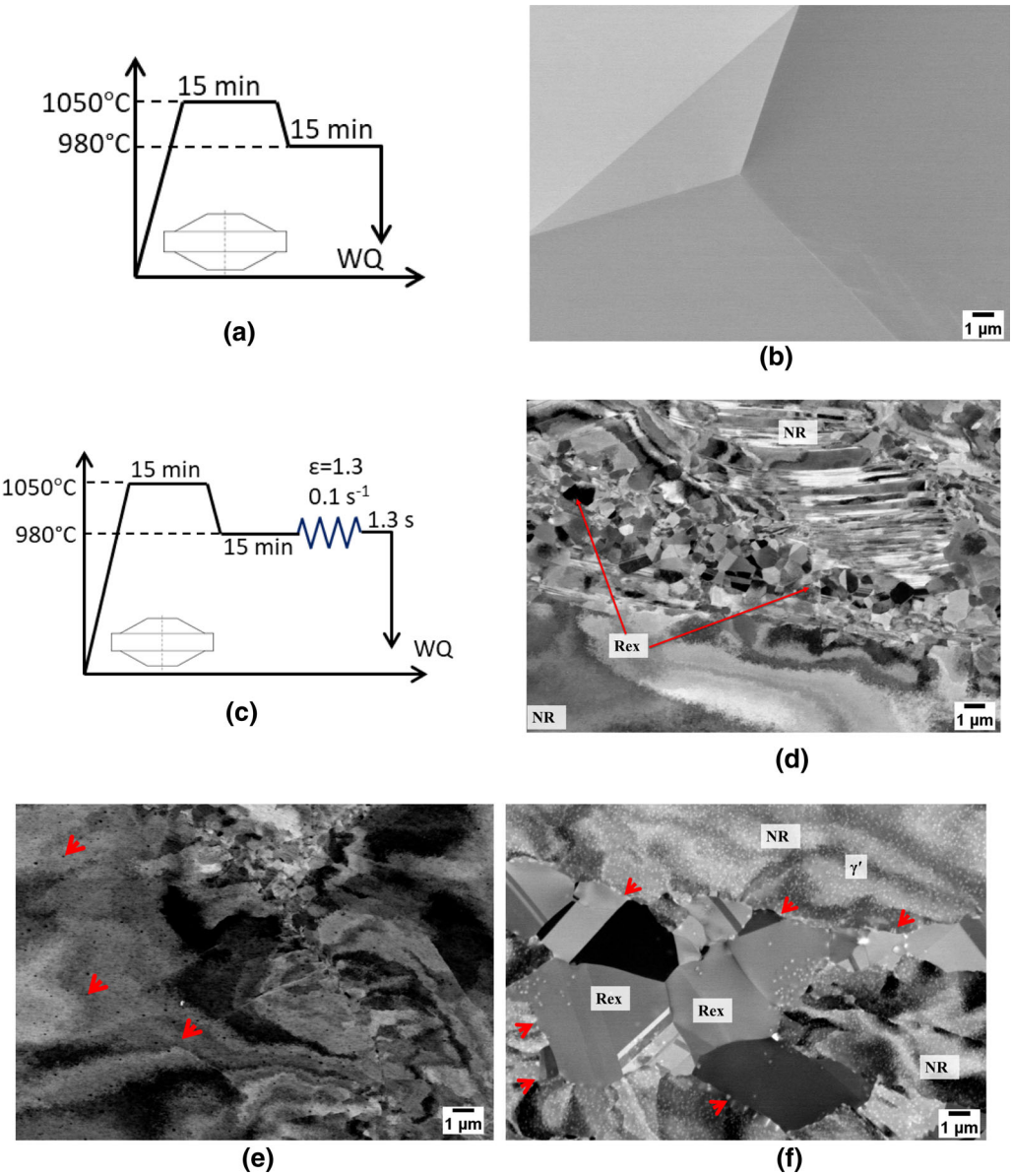


Fig. 15—(*a*) Extension of single-phase domain after 1050 °C–15 min–980 °C–15 min–WQ, (*b*) BSE image showing absence of second-phase particles, (*c*) Schematic representation of deformation on billet sample at 1050 °C–15 min–980 °C–15 min–0.1 $s^{-1}$–$\varepsilon$ = 1.3–WQ–QD = 1.3 s, (*d*, *e*) BSE images showing $\gamma'$ precipitates in the non-recrystallized grains, and (*f*) evolution of $\gamma'$ precipitates after adding a post-deformation hold of 5 min to (c). Microstructures obtained after electrolytic polishing in (f) and mechanical polishing in (b, d through e).

each temperature to release initial stored energy present in the as-received state and (ii) post-dynamically recrystallized samples with finer grain sizes (Table III).

As shown in Figure 1, the microstructure of as-received billet comprised remnant stored energy in addition to the fine $\gamma'$ precipitates. A hold of 15 minutes at 1050 °C, 1080 °C and 1120 °C was applied to release the remnant stored energy in the as-received billet material before proceeding to the (capillarity-driven) grain growth annealing. It is a useful precaution to accurately control the nature of the driving force leading to microstructure evolution when seeking to assess intrinsic properties of the alloy.

Grain growth is indeed defined as the process by which grain boundaries keep moving driven by capillarity forces which tend to reduce grain boundary curvature and lead to an increase in grain size after the stored energy in the microstructure has been consumed by the recrystallization processes. In the kinetics shown on Figure 16, the increase in grain size is initially faster when starting from an initially smaller grains size (PDRX microstructure compared to the billet material) because grain boundary curvature, and thus the grain growth driving force, is higher in finer grain microstructures.

For a given temperature, grain growth is slower in VDM Alloy 780 than in Alloy 718.[19] For example, the

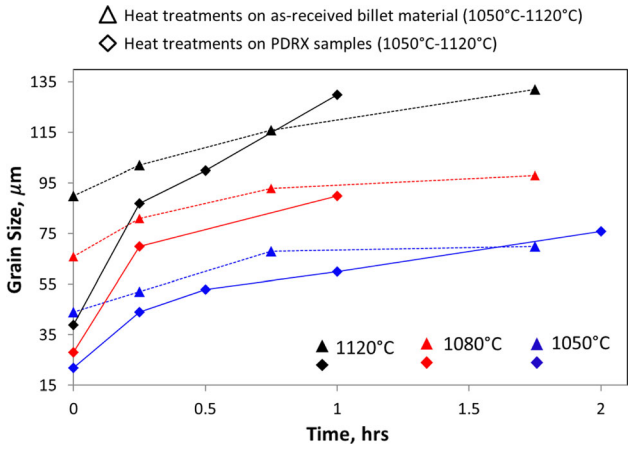


Fig. 16—Grain growth kinetics in VDM Alloy 780 in the temperature range 1050 °C to 1120 °C.

grain size increases from about 70 to about 130 $\mu$m in 45 minutes at 1080 °C in the Alloy 718, while it increases from about 65 to only 90 $\mu$m during the same time at the same temperature in the VDM Alloy 780.

The relatively slow kinetics can be advantageous to achieve finer grain sizes after forging and subsequent thermal treatments in the single-phase domain, *i.e.*, without second phase particles. Once microstructure is fully recrystallized, holding the material at elevated temperatures for longer times would lead to relatively slow and thus controllable capillarity driven grain growth. One of the possible explanations for this kind of slow grain growth kinetics could be chemical segregation of alloying elements at the grain boundaries. The effective grain boundary mobility would be reduced due to chemical segregation through solute drag effect.[41] On the other hand, apart from possible segregation effects on mobility, chemical composition is a factor which controls also grain boundary energy; lower grain boundary energy provides a lower curvature induced driving force and in turn leads to slower boundary migration. Such effects could be related to the high cobalt content (25 wt pct) in VDM Alloy 780 or to a combined effect of several alloying element, which remains to be confirmed through further dedicated investigations.

## IV. SUMMARY AND CONCLUSIONS

The recrystallization behavior of VDM Alloy 780 was studied in a temperature range of 1000 °C to 1120 °C, strain varying over 0.08 to 1.7 and using two nominal strain rates (0.01 and 0.1 $s^{-1}$). The necklace-type topology which is typical of discontinuous dynamic recrystallization and very common in polycrystalline nickel-based superalloys was observed, with the new recrystallized grains mostly found at the grain boundaries where the dislocation densities are relatively higher as compared to the grain interiors.

The microstructural evolution during dynamic regime was analyzed as a function of strain, strain rate and temperature. As expected, DRX fraction increased with both strain level and temperature. Lower strain rate (0.01 $s^{-1}$) resulted in a higher recrystallized fraction for a given strain level and temperature. However, at high temperatures, the sensitivity of recrystallization kinetics to strain rate became much weaker. The DRX grain sizes did not vary significantly with the applied strain rates at a given temperature and strain level.

Dynamic recrystallization kinetics in VDM Alloy 780 were shown to be slow, compared to Alloy 718 for example, but this is compensated by the fast post-dynamic evolution kinetics. Most of the deformation conditions, except for strain levels below 0.4, led to fully recrystallized microstructures after only 5 minutes isothermal holding after deformation. In addition, these fully recrystallized microstructures appeared to be almost independent of the prior deformation conditions (strain and strain rate) and related initial dynamically recrystallized fraction, but primarily on dependent temperature.

For strain levels in the range 0.08 to 0.4, an additional thermal treatment for 30 minutes at the tested deformation temperature of 1050 °C allowed to complete recrystallization even for the lowest strain levels, and to achieve again homogeneous grain size independent from the prior strain level applied and related dynamically recrystallized fraction. It should be pointed out here that the VDM Alloy 780 was thus shown to not be sensitive, at least at this temperature, to the heterogeneous grains size development phenomena which have been reported for many other nickel-based superalloys.

Once the microstructure is fully recrystallized (because of both dynamic and post-dynamic recrystallization), the grain size keep increasing slowly by capillarity driven grain growth, again dependent on temperature. Grain growth kinetics are also slower (about twice) than those of Alloy 718, which makes fine tuning of grain size easier in industrial conditions, meaning when short annealing times are not applicable.

The high cobalt content (25 pct) of VDM Alloy 780 resulting in reduced stacking fault energy could explain the slow dynamic recrystallization kinetics, by difficulty in the formation of nuclei, by hindering local recovery mechanisms. Cobalt and more generally chemical composition must somehow be also involved in the slow grain growth kinetics, by segregations or solute drag effects leading to low effective grain boundary mobility. The latter nevertheless does not prevent post-dynamic recrystallization to occur and to be fast, because it is then compensated by the high driving force associated with stored energy consumption and by time available for the completion of nuclei formation.

With recrystallized grain size primarily dependent on temperature and almost independent of the applied strain (including strains as low as 0.08) and of strain rate (within the range typical for hydraulic forging), the overall supersolvus recrystallization behavior of VDM Alloy 780 can be beneficial for the industrial forging processes where the deformation conditions are never uniform throughout the process and the piece. The

post-dynamic recrystallization behavior coupled with the slow grain growth behavior in VDM Alloy 780 provide control over the microstructural evolution and resulting grain sizes. These characteristics make VDM Alloy 780 suitable for forging in single phase domain, especially when applications require fine and uniform grain sizes.

## ACKNOWLEDGMENTS

The results presented in this paper have been taken from the PhD work of Juhi Sharma done at CEMEF—MINES ParisTech funded by VDM Metals International GmbH. The authors would like to thank the MSR technical staff members for their valuable help in conducting the experiments, G. Fiorucci for thermomechanical tests and C. Collin and S. Jacomet for metallographic characterization.

## CONFLICT OF INTEREST

The authors declare that they have no conflict of interest.

## OPEN ACCESS



## REFERENCES

1. T.M. Pollock and S. Tin: *J. Propul. Power*, 2006, vol. 22, pp. 361–74. https://doi.org/10.2514/1.18239.
2. J. Sharma, A. Nicolaÿ, M. De Graef, and N. Bozzolo: *Mater. Charact.*, 2021, vol. 176, pp. 1–9. https://doi.org/10.1016/j.matchar.2021.111105.
3. C. Ghica, C. Solis, J. Munke, A. Stark, B. Gehrmann, M. Bergner, J. Rosler, and R. Gilles: *J. Alloys Compd.*, 2020, https://doi.org/10.1016/j.jallcom.2019.152157.
4. C. Solis, J. Munke, M. Bergner, A. Kriele, M.J. Muhlbauer, D.V. Cheptiakov, B. Gehrmann, J. Rosler, and R. Gilles: *Metall. Mater. Trans. A*, 2018, vol. 49A, pp. 4373–81. https://doi.org/10.1007/s11661-018-4761-6.
5. C. Solis, J. Munke, M. Hofmann, S. Muhlbauer, M. Bergner, B. Gehrmann, J. Rosler, and R. Gilles: *Charact. Miner. Met. Mater.*, 2019, pp. 23–32. https://doi.org/10.1007/978-3-030-05749-7_3.
6. T. Fedorova, J. Rosler, B. Gehrmann, and J. Klower: in *Invention of a New 718-Type Ni-Co Superalloy Family for High Temperature Applications at 750°C*, Wiley, 2014. https://doi.org/10.1002/9781119016854.ch46.
7. T. Fedorova, J. Rosler, J. Klower, and B. Gehrmann: in *Proceedings of Eurosuperalloys*, 2014. https://doi.org/10.1051/matecconf/20141401003.
8. J. Rosler, T. Hentrich, and B. Gehrmann: *Metals*, 2019, vol. 9, pp. 1–20. https://doi.org/10.3390/met9101130.
9. J. Sharma, M. Hafez, B. Gehrmann, C. Moussa, and N. Bozzolo: in *Proceedings of the 14th International Symposium on Superalloys 2020*, pp. 450–60.
10. M.A. Charpagne, J.M. Franchet, and N. Bozzolo: *Mater. Des.*, 2018, vol. 144, pp. 353–60. https://doi.org/10.1016/j.matdes.2018.02.048.
11. M. BrozovicGariglio, N. Bozzolo, and D. Pino Muñoz: *Metall. Mater. Trans. A*, 2021, vol. 52A, pp. 4125–36. https://doi.org/10.1007/s11661-021-06373-8.
12. F. Bachmann, R. Hielscher, and H. Schaeben: *Ultramicroscopy*, 2011, vol. 111, pp. 1720–33. https://doi.org/10.1016/j.ultramic.2011.08.002.
13. A. Seret, C. Moussa, M. Bernacki, J. Signorelli, and N. Bozzolo: *J. Appl. Crystallogr.*, 2019, vol. 52, pp. 548–63. https://doi.org/10.1107/S1600576719004035.
14. A. Nicolaÿ, J.M. Franchet, J. Cormier, H. Mansour, M. de Graef, A. Seret, and N. Bozzolo: *J. Microsc.*, 2019, vol. 273, pp. 135–47. https://doi.org/10.1111/jmi.12769.
15. K. Chen, J. Wu, H. Shi, X. Chen, Z. Shen, M. Zhang, L. Zhang, and A. Shan: *Mater. Charact.*, 2015, vol. 106, pp. 175–84. https://doi.org/10.1016/j.matchar.2015.05.034.
16. D. Li, Q. Guo, S. Guo, H. Peng, and Z. Wu: *Mater. Des.*, 2011, vol. 32, pp. 696–705. https://doi.org/10.1016/j.matdes.2010.07.040.
17. E. Eriksson and M.H. Colliander: *Metals*, 2021, vol. 11, pp. 1–24. https://doi.org/10.3390/met11010122.
18. Y.C. Lin, X.Y. Wu, X.M. Chen, J. Chen, D.X. Wen, J.L. Zhang, and L.T. Li: *J. Alloys Compd.*, 2015, vol. 640, pp. 101–13. https://doi.org/10.1016/j.jallcom.2015.04.008.
19. M. Zouari, N. Bozzolo, and R.E. Logé: *Mater. Sci. Eng. A*, 2016, vol. 655, pp. 408–24. https://doi.org/10.3390/met7110476.
20. M. Zouari, R.E. Logé, and N. Bozzolo: *Metals*, 2017, vol. 7, p. 476. https://doi.org/10.3390/met7110476.
21. A. Nicolay, G. Fiorucci, J.M. Franchet, J. Cormier, and N. Bozzolo: *Acta Mater.*, 2019, vol. 174, pp. 406–17. https://doi.org/10.1016/j.actamat.2019.05.061.
22. N. Bozzolo and M. Bernacki: *Metall. Mater. Trans. A*, 2020, vol. 51A, pp. 2665–84. https://doi.org/10.1007/s11661-020-05772-7.
23. T. Sakai, A. Belyakov, R. Kaibyshev, H. Miura, and J.J. Jonas: *Prog. Mater. Sci.*, 2014, vol. 60, pp. 130–207. https://doi.org/10.1016/j.pmatsci.2013.09.002.
24. A. Belyakov, W. Gao, H. Miura, and T. Sakai: *Metall. Mater. Trans. A*, 1998, vol. 29A, pp. 2957–65. https://doi.org/10.1007/s11661-998-0203-1.
25. X.M. Chen, Y.C. Lin, D.X. Wen, J.L. Zhang, and M. He: *Mater. Des.*, 2014, vol. 57, pp. 568–77. https://doi.org/10.1016/j.matdes.2013.12.072.
26. A. Momeni, S.M. Abbasi, M. Morakabati, and H. Badri: *Metall. Mater. Trans. A*, 2017, vol. 48A, pp. 1216–29. https://doi.org/10.1016/j.msea.2014.07.060.
27. J.Y. Song, S. Sato, Y. Koizumi, and A. Chiba: *Adv. Mater. Res.*, 2014, vol. 922, pp. 711–15. https://doi.org/10.4028/www.scientific.net/amr.922.711.
28. Y. Yuan, Y. Gu, C. Cui, T. Osada, Z. Zhong, T. Tetsui, T. Yokokawa, and H. Harada: *J. Mater. Res.*, 2011, vol. 26, pp. 2833–37. https://doi.org/10.1557/jmr.2011.346.
29. C. Kienl: Hot forging of the nickel-base superalloy ATI 718Plus, PhD thesis, University of Cambridge, 2019.
30. D. Jia, W. Sun, D. Xu, L. Yu, X. Xin, W. Zhang, and F. Qi: *J. Alloys Compd.*, 2019, vol. 787, pp. 196–205. https://doi.org/10.1016/j.jallcom.2019.02.055.

31. D. Zhao and P.K. Chaudhury: *Superalloys 718*, 1994, vol. 625, pp. 303–313.
32. M. Azarbarmas, M. Aghaie-Khafri, J.M. Cabrera, and J. Calvo: *Mater. Des.*, 2016, vol. 94, pp. 28–38. https://doi.org/10.1016/j.matdes.2015.12.157.
33. H. Zhang, K. Zhang, H. Zhou, Z. Lu, C. Zhao, and X. Yang: *Mater. Des.*, 2015, vol. 80, pp. 51–62. https://doi.org/10.1016/j.matdes.2015.05.004.
34. S.S.S. Kumar, T. Raghu, P.P. Bhattacharjee, G.A. Rao, and U. Borah: *J. Alloys Compd.*, 2016, vol. 681, pp. 28–42. https://doi.org/10.1016/j.jallcom.2016.04.185.
35. H. Jiang, J. Dong, M. Zhang, and Z. Yao: *Metall. Mater. Trans. A.*, 2016, vol. 47A, pp. 5071–87. https://doi.org/10.1007/s11661-016-3664-7.
36. N.R. Jaladurgam and A.K. Kanjarla: *Mater. Sci. Eng. Aa*, 2018, vol. 712, pp. 240–54. https://doi.org/10.1016/j.msea.2017.11.056.
37. Z. Shi, X. Yan, C. Duan, and M. Zhao: *Trans. Nonferrous Met. Soc. China.*, 2017, vol. 27, pp. 538–50. https://doi.org/10.1016/S1003-6326(17)60082-7.
38. Y. Fang, X. Chen, B. Madigan, H. Cao, and S. Konovalov: *Fusion Eng. Des.*, 2016, vol. 103, pp. 21–30. https://doi.org/10.1016/j.fusengdes.2015.11.036.
39. S. Mandal, A.K. Bhaduri, and V.S. Sarma: *Metall. Mater. Trans. A.*, 2012, vol. 43A, pp. 2056–68. https://doi.org/10.1007/s11661-011-1012-5.
40. Y. Cao, H. Di, J. Zhang, J. Zhang, T. Ma, and R.D.K. Misra: *Mater. Sci. Eng. A*, 2013, vol. 585, pp. 71–85. https://doi.org/10.1016/j.msea.2013.07.037.
41. F. Humphreys and M. Hatherly: *Recrystallization and Related Annealing Phenomena*, 2nd ed., Elsevier, Amsterdam, 2004.
42. V.M. Miller, A.E. Johnson, C.J. Torbet, and T.M. Pollock: *Metall. Mater. Trans. A*, 2016, vol. 47A, pp. 1566–74. https://doi.org/10.1007/s11661-016-3329-6.
43. A. Agnoli, M. Bernacki, R. Logé, J.M. Franchet, J. Laigo, and N. Bozzolo: *Metall. Mater. Trans. A*, 2015, vol. 46A(9), pp. 4405–421. https://doi.org/10.1007/s11661-015-3035-9.
44. D. Raabe: in *Phenomena, Physics, Models, Simulation*, 5th ed., Elsevier, Amsterdam, 2014.
45. E. Huron, S. Srivatsa, and E. Raymond: in *Proceedings of Superalloys*, 2000, pp. 49–58.
46. I.M.D. Parr, T.J. Jackson, M.C. Hardy, D.J. Child, C. Argyrakis, K. Severs, V. Saraf, and J.M. Stumpf: in *Proceedings of 13th International Symposium on Superalloy 718*, 2016, pp. 447–56.
47. D.D. Whitis: in *Proceedings of Superalloys*, 2004, pp. 391–400.
48. A. Seret, C. Moussa, M. Bernacki, and N. Bozzolo: *Metall. Mater. Trans. A*, 2018, vol. 49A, pp. 4199–213. https://doi.org/10.1007/s11661-018-4707-z.
49. G. Sauthoff: *J. Phys. IV*, 1996, vol. 6, pp. C1–87–97.
50. M. Legros, G. Dehm, E. Arzt, and T.J. Balk: *Science*, 2008, vol. 319, pp. 1646–49. https://doi.org/10.1126/science.1151771.